Journal of Cerebral Blood Flow and Metabolism
12:571–583 © 1992 The International Society of Cerebral Blood Flow and Metabolism
Published by Raven Press, Ltd., New York

Measurement of Radiotracer Concentration in Brain Gray Matter Using Positron Emission Tomography: MRI-Based Correction for Partial Volume Effects

*Hans W. Müller-Gärtner, *Jonathan M. Links, §Jerry L. Prince, †R. Nick Bryan, †Elliot McVeigh, *Jeffrey P. Leal, §Christos Davatzikos, and *‡J. James Frost

**Department of Radiology, Division of Nuclear Medicine, †Department of Radiology, Division of Neuroradiology, and ‡Department of Neuroscience, The Johns Hopkins University School of Medicine, and §Department of Electrical and Computer Engineering, The Johns Hopkins University, Baltimore, Maryland, U.S.A.*

Summary: Accuracy in in vivo quantitation of brain function with positron emission tomography (PET) has often been limited by partial volume effects. This limitation becomes prominent in studies of aging and degenerative brain diseases where partial volume effects vary with different degrees of atrophy. The present study describes how the actual gray matter (GM) tracer concentration can be estimated using an algorithm that relates the regional fraction of GM to partial volume effects. The regional fraction of GM was determined by magnetic resonance imaging (MRI). The procedure is designated as GM PET. In computer simulations and phantom studies, the GM PET algorithm permitted a 100% recovery of the actual tracer concentration in neocortical GM and hippocampus, irrespective of the GM volume. GM PET was applied in a test case of temporal lobe epilepsy revealing an increase in radiotracer activity in GM that was undetected in the PET image before correction for partial volume effects. In computer simulations, errors in the segmentation of GM and errors in registration of PET and MRI images resulted in less than 15% inaccuracy in the GM PET image. In conclusion, GM PET permits accurate determination of the actual radiotracer concentration in human brain GM in vivo. The method differentiates whether a change in the apparent radiotracer concentration reflects solely an alteration in GM volume or rather a change in radiotracer concentration per unit volume of GM. **Key Words:** Brain gray matter—Positron emission tomography—Magnetic resonance imaging—Partial volume effects—Aging—Dementia—Brain atrophy.

Positron emission tomography (PET) permits investigation of physiological and biochemical processes in human brain in vivo, and has yielded new insights into both normal physiology and diseases (Kuhl et al., 1982; Foster, 1983; Wagner et al., 1983; Frost et al., 1985; Phelps and Mazziotta, 1985; Frost, 1986; Yamaguchi et al., 1986; Yoshii et al., 1988; Fowler, 1990; Frost and Wagner, 1990; Leenders et al., 1990; Martin et al., 1991; Mayberg et al., 1991). Nevertheless, a limitation of PET remains: its relatively poor spatial resolution. As a result, PET quantification, especially in structures smaller than two times the full width at half-maximum (FWHM) of the tomograph, is affected by partial volume effects (Hoffmann et al., 1979). Given that the in-plane FWHM of current PET instruments ranges from 2.6 mm (Valk et al., 1990) to about 14 mm, tracer activity in many brain structures, including the neocortex, is often underestimated. In neocortex, gray matter (GM), white matter (WM), and cerebrospinal fluid (CSF) spaces are convoluted, and cannot be resolved using PET instrumentation; a cortical PET signal thus reflects the average tracer concentration in all three compartments.

Received September 16, 1991; final revision received November 21, 1991; accepted November 26, 1991.

Address correspondence and reprint requests to Dr. J. J. Frost at The Johns Hopkins University School of Medicine, Department of Radiology, Room B1—130, 600 North Wolfe Street, Baltimore, MD 21205, U.S.A.

Abbreviations used: AU, arbitrary units; FWHM, full width at half-maximum; GM, gray matter; MRI, magnetic resonance imaging; PET, positron emission tomography; RMSE, relative mean-squared error; ROI, region of interest; SPGR, spoiled grass; WM, white matter.

Similarly, tracer concentrations are underestimated in subcortical GM structures such as the caudate nucleus and amygdala as the result of limited spatial resolution.

The relative percentage of GM, WM, and CSF may vary regionally in the same subject and between subjects, particularly as a result of aging or disease, and therefore any given change in the apparent tracer concentration in PET may reflect a change in morphology rather than in physiology or biochemistry. The importance of developing algorithms to compensate for partial volume effects in PET studies is well recognized (Chawluk et al., 1990; Martin et al., 1991; Rabins et al., 1991). In the past, phantoms were employed to correct for partial volume effects in selected brain structures (Kessler et al., 1984; Müller-Gärtner et al., 1991). This is a tedious approach that produces data for a few regions under particular conditions.

Previous attempts to correct PET images for partial volume effects used x-ray computed tomography (CT) (Herscovitch et al., 1986; Chawluk et al., 1987) and focussed on partial volume effects due to CSF. The limitations of these methods have been discussed (Penn et al., 1978; Wyper et al., 1979; Koeppe et al., 1989). A method for correcting PET images on a pixel-by-pixel basis in two dimensions for partial volume effects due to CSF was described by Videen et al. (1988), using high resolution CT or magnetic resonance imaging (MRI). In this approach, anatomic images are used to create a brain tissue image by assigning brain pixels a value of 1 and pixels representing CSF a value of 0. These images are then convolved with the two-dimensional Gaussian point spread function of the PET scanner to create a corrected tissue image. The PET image is subsequently divided by the corrected tissue image on a pixel-by-pixel basis to yield a corrected PET image in which pixels represent activity per actual brain tissue volume (GM *and* WM) rather than per unit spatial volume. This method was extended to three dimensions through the use of standard MRI T_2-weighted pulse sequences (Meltzer et al., 1990*a*), which provide greater accuracy in quantitative measures of brain atrophy (Condon et al., 1986; Seab et al., 1988; Kohn et al., 1991; Tanna et al., 1991).

The approaches reported by Videen et al. (1988) and Meltzer et al. (1990*a*) targeted partial volume effects due to varying CSF content without distinction between GM and WM. We now describe a method that addresses partial volume effects specifically in GM. The method is presented with an analytical theory, and includes computer simulations and phantom studies for validation. The procedure is designated as GM PET, in which an image reflects tracer concentration per unit volume of GM, rather than per unit volume of brain tissue.

METHODS

Theory

The observed PET image (I_{obs}) is the convolution ($\otimes$) of the actual radioactivity distribution (I_{actual}) and the three-dimensional point spread function (h) of the system:

$$I_{obs} = I_{actual} \otimes h \tag{1}$$

I_{actual} is the linear sum of the images of GM (I_{gray}), WM (I_{white}), and CSF (I_{CSF}):

$$I_{actual} = I_{gray} + I_{white} + I_{CSF} \tag{2}$$

From Eqs. (1) and (2), noting that convolution is a linear operator,

$$I_{obs} = I_{gray} \otimes h + I_{white} \otimes h + I_{CSF} \otimes h \tag{3}$$

It is assumed that the radioactivity concentration within WM ($\bar{I}_{white}$) and CSF ($\bar{I}_{CSF}$) is constant and known. The spatial location (characteristic function) of GM (X_{gray}), WM (X_{white}), and CSF (X_{CSF}) is known from MRI; $X_{tissue} = 1$ for pixels representing that tissue, and zero otherwise:

$$\begin{aligned} I_{white} &= \bar{I}_{white} X_{white} \\ I_{CSF} &= \bar{I}_{CSF} X_{CSF} \end{aligned} \tag{4}$$

I_{gray} is the unknown, and is given by

$$I_{gray} = \tilde{I}_{gray} X_{gray} \tag{5}$$

$\tilde{I}_{gray}$ indicates that the concentration within GM is not assumed to be uniform. I_{gray} and $\tilde{I}_{gray}$ are actually the same, except $\tilde{I}_{gray}$ is undefined for pixels not in GM, whereas X_{gray} explicitly sets $I_{gray} = 0$ for pixels not in gray matter. It then follows by substitution that

$$\begin{aligned} I_{obs} = I_{gray} \otimes h + \bar{I}_{white} X_{white} \otimes h \\ + \bar{I}_{CSF} X_{CSF} \otimes h \end{aligned} \tag{6}$$

Rearranging,

$$\begin{aligned} I_{gray} \otimes h = I_{obs} - \bar{I}_{white} X_{white} \otimes h \\ - \bar{I}_{CSF} X_{CSF} \otimes h \end{aligned} \tag{7}$$

Equation (8) results from Eq. (5):

$$I_{gray} \otimes h = (\tilde{I}_{gray} X_{gray}) \otimes h \tag{8}$$

Then, under the condition that

$$(\tilde{I}_{gray} X_{gray}) \otimes h = \tilde{I}_{gray} (X_{gray} \otimes h) \tag{9}$$

the following expression results:

$$\begin{aligned} \tilde{I}_{gray} = (I_{obs} - \bar{I}_{white} X_{white} \otimes h \\ - \bar{I}_{CSF} \otimes h)/X_{gray} \otimes h \end{aligned} \tag{10}$$

The condition given in Eq. (9) is true when either h is a delta function or $\tilde{I}_{gray}$ is a constant, but is not true in general. Therefore, the expression given in Eq. (10) provides an estimate of $\tilde{I}_{gray}$. It is demonstrated both in simulation and phantom experiments in this report, however,

that this estimate is a very good one in typical cortical PET imaging scenarios.

Implementation

The implementation of an MRI-based correction map involves smoothing segmented MRI data to the effective resolution of the PET data. h, the three-dimensional point spread function of the PET scanner, was measured with a point source (diameter < 1 mm) in water. In-plane resolution (13 mm) and axial resolution (14.5 mm) were not identical. Three-dimensional convolution of the MRI data would thus have required the use of an asymmetric three-dimensional point spread function. Such a process would have produced a complete set of convolved MRI slices spanning the original MRI axial field. Since we were only interested in obtaining that single convolved MRI slice coplanar with the PET image, for computational efficiency we chose instead to perform the three-dimensional convolution in two serial convolution steps. We utilized 9 (slice thickness of 3 mm) or 17 (slice thickness of 1.5 mm) MRI slices, 1 coplanar with the PET slice, and 4 or 8 on either side of the slice in the axial direction. Axial convolution was performed by weighted summation of these MRI images, according to their axial position relative to the axial point spread function. The resulting image was then convolved with the in-plane point spread function (15 × 15 kernel), which produced a convolved MRI image with the same three-dimensional resolution as the PET image.

I_{obs} is the acquired PET scan. X_{tissue} is determined from trisegmented MRI and $\bar{I}_{tissue}$ is determined from a large region of interest (ROI) for WM (centrum semiovale) and CSF in the PET scan. In practice, the pixel values within the trisegmented MRI are modified as follows: all WM MRI pixel values are replaced by the average WM PET counts and all CSF MRI pixel values are replaced by the average CSF PET counts. GM MRI pixel values are replaced by 0. This modified MRI image is then convolved with h, and, because of Eq. (2) and the linear nature of convolution, represents

$$I_{MR_{mod}} = \bar{I}_{white} X_{white} \otimes h + \bar{I}_{CSF} X_{CSF} \otimes h \quad (11)$$

The pixel size of MRI images is adjusted to the pixel size of the PET image. $I_{MR_{mod}}$ is then subtracted from the observed PET image I_{obs} to yield

$$I_{PET_{mod}} = I_{obs} - I_{MR_{mod}} = I_{gray} \otimes h \quad (12)$$

The original trisegmented MRI is then modified again, as follows: all WM and CSF pixel values are replaced by 0, and all GM pixel values are replaced by 1. This modified MRI image is then convolved with h, and represents

$$I_{MR_{mod'}} = X_{gray} \otimes h \quad (13)$$

Finally, based on Eq. (10), the modified PET image is divided by this modified MRI image to yield the estimate

$$\bar{I}_{gray} = I_{PET_{mod}} / I_{MR_{mod'}} \quad (14)$$

MRI image convolution was performed on an IBM PC clone with an 80386 CPU and 80387 math coprocessor using custom developed software. The remaining image processing (i.e., segmentation, thresholding, and quantification) was performed on a Macintosh computer image analysis system (Digital Image Processing Station, version 1.0.2, Hayden Image Processing Group and William Connor, Cleveland, OH, U.S.A.). The application of the computer analysis on a given data set ranged between 60 and 90 min.

Positron emission tomography

PET studies were performed on a Neuro-ECAT scanner (CTI, Knoxville, TN, U.S.A.). The z axis FWHM is 14.5 mm. Scans were performed in the high-resolution mode with an in-plane FWHM of 8 mm. Images were reconstructed with a 100 × 100 matrix of 2.77 × 2.77 mm pixels. The PET data were corrected for attenuation (by calculation) and radioactive decay. Smoothing, using a 9 × 9 weighted filter, yielded a final image with an in-plane FWHM of 13 mm. The scans on the human subject were acquired over 90 min following intravenous injection of 740 MBq (20 mCi) of [^{11}C]carfentanil (Frost et al., 1985). Images were summed over the interval 35–70 min after injection.

Magnetic resonance imaging

MRI scans were acquired on a 1.5 T scanner (Signa, General Electric, Milwaukee, WI, U.S.A.). A spoiled grass (SPGR) pulse sequence (65, 5, 45, 2; TR, TE, flip angle, NEX) was used in volume mode. The field of view was 24 × 24 cm and the reconstruction matrix was 256 × 256 pixels, resulting in a final in-plane pixel size of 0.94 × 0.94 mm. The number of slices was 32 or 64, and the slice thickness was 1.5 or 3 mm.

The phantoms were aligned in the MRI scanner such that the imaging plane, as indicated by a laser light, passed through the centers of the spheres and the brain phantom. For the human studies, an imaging plane for the PET study was selected from a sagittal T_1-weighted MRI image (600, 20, 1; TR, TE, NEX; slice thickness of 5 mm, interslice gap of 1.5 mm). A line coincident with the selected imaging plane was drawn on an individually fitted, thermoplastic mask (Polysplint, Poly-Med Manufacturing Co., Baltimore, MD, U.S.A.) for subsequent alignment during the PET study, as previously described (Meltzer et al., 1990*b*). A set of contiguous 1.5 mm thick transaxial images in the above-described SPGR mode was acquired parallel to this plane.

MRI brain tissue segmentation

To segment brain tissue into GM, WM, and CSF, a ROI covering all three compartments was drawn, resulting in a composite of distributions. The resulting histogram was smoothed by averaging a neighborhood of 11 data points. Peaks were identified by determining local maxima. Normal distributions were then fitted to the identified peaks using a minimization procedure of the relative mean-squared error (RMSE) defined as

$$\text{RMSE} = \frac{\sum_{i=1}^{k} (\Delta x_i)^2}{\sum_{i=1}^{k} x_i^2} \quad (15)$$

where k corresponds to the number of signal intensity classes, and Δx_i to the estimation error, defined as $f_i - x_i$, where f_i represents the Gaussian distribution. x_i is the measured number of pixels with a given signal intensity. Each pixel was thereafter identified as either GM, WM, or CSF using a minimum probability of error decision rule

(Van Trees, 1968). This classification procedure yields the required image segmentation.

The contrast between WM and GM was defined as the difference between the signal intensity in GM and WM divided by the noise. Noise was measured as the standard deviation of the background signal intensity divided by 0.655 (Henkelman, 1985).

Computer simulations

These experiments involved (a) acquisition of human MRI data, (b) segmentation of the MRI data into GM, WM, and CSF, (c) assignment of tracer concentrations to GM, WM, and CSF, (d) generation of a simulated PET image, and (e) partial volume correction of the simulated PET image using segmented MRI data.

Contiguous transaxial MRI images of a patient with moderately advanced Alzheimer disease were coded as follows (Fig. 1): pixels representing CSF were set to 0, and WM (blue) to 40 arbitrary units (AUs); pixels depicting GM were set to 120 (green, normal GM), 160 (yellow, amygdala), or 240 AU (red, region of focally increased cortical tracer uptake) (Fig. 1a). Whereas the red cortical area was present in all coded MRI slices, the amygdala were coded only in the five middle slices.

This coded MRI three-dimensional data set was first used to generate a single simulated PET image (I_{obs}). The MRI images were multiplied by a weighting factor according to their axial position relative to the axial point spread function of the PET scanner, axially centered on the middle slice. The weighting factors summed to 1. These scaled images were then summed; the resulting image represented an axially smoothed slice. This image was then convolved with the two-dimensional (in-plane) point spread function of the PET scanner. The resulting simulated PET image was equivalent to that which would have been produced from three-dimensional convolution with a three-dimensional point spread function [as in Eq. (1)].

This simulated PET image was then "corrected" for partial volume effects as follows: First, the same weighted summing and convolution process was applied to a WM only data set (WM = 40 AU; GM and CSF = 0) to produce $I_{MR_{mod}}$ [as in Eq. (11)] and a GM only data set (GM = 1; WM and CSF = 0) to produce $I_{MR_{mod'}}$ [as in Eq. (13)]. The modified WM image was subtracted from the simulated PET image. The latter was subsequently divided by the modified GM image to produce the GM PET image [as in Eqs. (12) and (14)].

A ROI template was drawn on the weighted summed GM MRI image such that each ROI was centered on the greatest GM density. This template was transferred onto the registered simulated PET image (Fig. 1b) as well as onto the GM PET image (Fig. 1f).

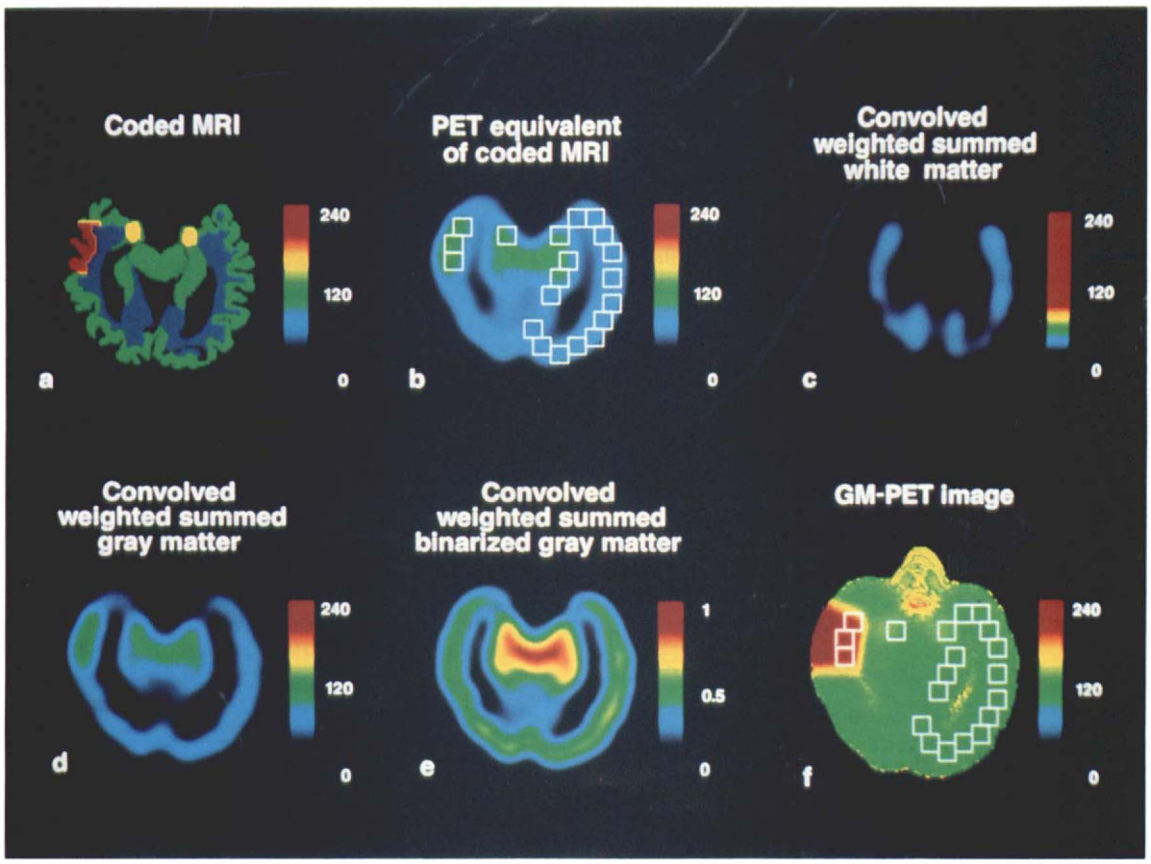

FIG. 1. Computer simulation of GM PET using coded MRI images of a patient with Alzheimer disease. Values in Fig. 1a–1d and 1f are displayed in arbitrary counts/pixel. Values in Fig. 1e are units of weighted gray matter density. **(a)** Coded MRI image, simulating the actual radiotracer distribution in two dimensions. **(b)** Simulated PET image, revealing a considerably lower tracer concentration in gray matter when compared to Fig. 1b. **(c)** Convolved weighted summed white matter image. **(d)** Convolved weighted summed gray matter image. **(e)** Convolved weighted summed binarized gray matter image. A value of 1 indicates that all coded MRI images consist of gray matter. **(f)** GM PET image. Result of dividing image 1d by image 1e.

Error analysis

To simulate the effects of missegmentation in GM PET, the nine coded MRI images used to create the convolved weighted summed WM image ($I_{MR_{mod}}$) and the convolved weighted summed binarized GM image ($I_{MR_{mod'}}$) were missegmented as follows: The actual edge between GM and WM was moved 1, 2, or 3 pixels into the GM compartment and subsequently into the WM compartment. The coded MRI images used to create the simulated observed PET image remained unchanged. The images were processed as described above. ROI templates were drawn on the missegmented weighted summed GM image and transferred onto the GM PET image.

To simulate the impact of a misdetermination of the actual tracer concentration in WM, the WM tracer concentration in the nine coded MRI images was increased and decreased by 10, 30, and 50% before creating the convolved weighted summed WM image ($I_{MR_{mod}}$).

The effect of misregistration of PET and MRI images was simulated by moving the convolved weighted summed WM image ($I_{MR_{mod}}$) and the convolved weighted summed binarized GM image ($I_{MR_{mod'}}$) concordantly 2, 3, or 5 pixels horizontally in the matrix, keeping the position of the simulated observed PET image (I_{obs}) constant. A movement of a cortical hemisphere towards the center of the observed PET image is referred to as centripetal misregistration, and the opposite as centrifugal misregistration. ROI templates were drawn on the misregistered weighted summed binarized GM image.

The impact of cortical inhomogeneity on the accuracy of GM PET was evaluated in computer simulations using the same coded MRI image approach as described above. The actual tracer concentration in the areas of focal cortical increase was 160 counts/pixel and in the surrounding neocortex was 120 counts/pixel. The size of the areas of cortical tracer increase ranged from 0.6 to 5.5 cm in the anterior–posterior and z axis dimension, and the thickness of the cortical gray matter was 5–7 mm. The areas of focal tracer increase were positioned in the center of the simulated PET image. The ROI size was 0.8 × 0.8 cm, centered on the area of focal increase in the weighted summed GM image, and transferred onto the GM PET image. The images were processed as described above.

Phantom experiments

Sphere phantom. Six fillable spheres with inner diameters of 3.8, 7.7, 8.1, 10.4, 15.7, and 28.0 mm were mounted in a cylindrical phantom (volume of 6.2 L, Data Spectrum Corp., Chapel Hill, NC, U.S.A.) filled with nonradioactive water. The rods attaching the spheres to the bottom plate of the cylinder were of the appropriate length (12.5 cm) such that the equators of the spheres were all in a single transverse plane. The spheres contained an ^{18}F solution (518 kBq/ml = 14 μCi/ml at scanning time) and were scanned such that the imaging plane, as indicated by a laser light, passed through the centers of the spheres. To account for any differences between the measured and the actual centers, the scan was repeated ±1 and ±2 mm from the measured centers. The plane with the maximum count rate per sphere was chosen for analysis (see Fig. 5a). Prior experiments had shown that an activity concentration of 518 kBq/ml was well in the linear range of the PET scanner's response. The same phantom without spheres was filled with an ^{18}F solution (118 kBq/ml = 3.2 μCi/ml) and scanned to provide the reference for computing the recovery coefficients of the spheres (full recovery PET image, see Fig. 5b). Data were decay corrected and normalized to the activity concentration and scan duration.

Subsequently, the spheres were filled with a 4 mM Cu_2SO_4 solution surrounded by a 1 mM Cu_2SO_4 solution and scanned in the MRI scanner. The MRI images were binarized (spheres = 1, background = 0) and added as follows: Each image was weighted according to its axial position by the z axis point spread function of the PET scanner. The summed image was then convolved with the two-dimensional point spread function of the PET scanner (see Fig. 5c).

Agarose cortex brain phantom. A brain phantom was constructed using agarose as brain tissue equivalent (Mitchell et al., 1986). The phantom consisted of three compartments representing GM, WM, and CSF. The surfaces between the compartments were approximately 5° off the plane perpendicular to the transaxial plane of the phantom. Each compartment was filled with a 1% (w/v) agarose matrix (A-6013 agarose type I, Sigma, St. Louis, MO. U.S.A.). The WM compartment also contained 0.02 mM $GdCl_3 \cdot 6H_2O$ and 30 kBq/ml (0.81 μCi/ml) of ^{18}F, and the GM compartment a 0.01 mM $GdCl_3 \cdot 6H_2O$ and 148 kBq/ml (4 μCi/ml) of ^{18}F. The CSF compartment did not contain any ^{18}F or $GdCl_3 \cdot 6H_2O$. In order to prevent diffusion, the compartments were separated using polyvinylacetate film (thickness <0.1 mm) and the edges were sealed with wax. The tightness of the seals was tested and confirmed by filling the compartments with a dye solution (azur II, EM Science, Cherry Hill, NJ, U.S.A.). The polyvinylacetate film itself was invisible on MRI scans of the same brain phantom when all three compartments contained 1% agarose gel, but no $GdCl_3 \cdot 6H_2O$. Appropriate concentrations of $GdCl_3 \cdot 6H_2O$ and ^{18}F concentrations were determined in prior experiments, showing a linear response of the MRI sequence for concentrations between 0.01 and 0.1 mM $GdCl_3 \cdot 6H_2O$ and a linear response of the PET device for less than 37 MBq (1 mCi) per field of view and less than 518 kBq/ml (14 μCi/ml). Homogeneous tracer distribution within each compartment was achieved by dissolving $GdCl_3 \cdot 6H_2O$ and ^{18}F in hot agarose (75°C). The diameter of the phantom was 11.7 cm, and the height was 6 cm. The smallest distance between the two polyvinylacetate films was 2 mm, and the largest was 20 mm.

The corresponding MRI images were segmented into CSF, WM, GM, and subsequently coded as follows: GM and WM were binarized (GM = 1, CSF = 0). WM pixels were set to 3,805 units/pixel, corresponding to the measured mean count rate in WM in the observed PET image of the phantom [see Eqs. (11) and (12)]. The observed PET image was corrected with the modified MRI images of WM and GM as described above.

RESULTS

Computer simulations

Processing of coded MRI images (see Fig. 1a) as described above resulted in the simulated observed PET image (I_{obs}) (see Fig. 1b). This image revealed a 28 to 53% lower tracer concentration when compared with the actual concentration (Fig. 2). The underestimation varied regionally, being smallest in hippocampus and highest in the area of focal increase of tracer uptake. Images required to perform

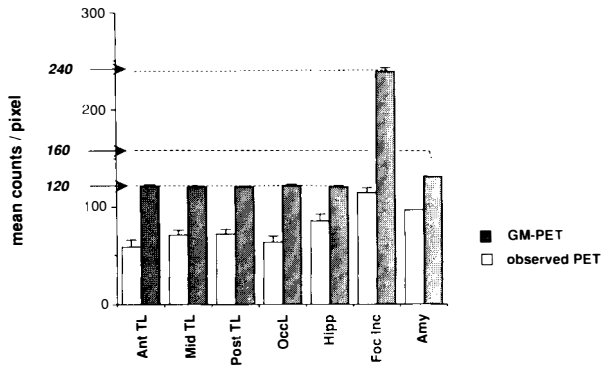

FIG. 2. Region-of-interest (ROI) analysis of simulated PET and GM PET images using coded MRI images in Alzheimer disease. The ROI template is shown in Fig. 1. Values are given as mean counts/pixel (±1 SD) from three ROIs in the anterior temporal lobe (Ant TL), the middle temporal lobe (Mid TL), posterior temporal lobe (Post TL), the occipital lobe (OccL), the hippocampus (Hipp), the area of focal increase in tracer uptake (Foc Inc), and one ROI over each amygdala (Amy). Figures in italics on the *y* axis indicate the actual tracer concentration in the coded MRI images. In the simulated PET image, the actual tracer concentration in cortex and amygdala was underestimated from 28% in hippocampus to 53% in the area of focal increase in tracer uptake. In the GM PET image, the actual tracer concentration was completely recovered in all cortical regions (including the area of focal increase in tracer uptake) and in hippocampus, to 82% in the amygdala.

the partial volume correction are shown in Fig. 1c ($I_{MR_{mod}}$), Fig. 1d ($I_{PET_{mod}}$), and Fig. 1e ($I_{MR_{mod}}$). The resulting GM PET image is depicted in Fig. 1f. The GM PET image looks similar to the GM compartment in the coded MRI image (see Fig. 1a), both in normal neocortex and in the area of focal increase. The tracer concentration in normal neocortex and hippocampus was almost identical to the actual value of 120. The variance was reduced from 8.2 ± 2.4% to 1.0 ± 0.2% (mean ± SD). Eighty-five percent of the actual amygdala concentration was recovered in the GM PET image. WM and CSF areas in the simulated GM PET reflect the tracer concentration of GM (see Fig. 1f). As shown in Table 1, a progressive increase of ROI size from 3 × 3 to 16 × 16 MRI pixels resulted in a gradual decline in the measured tracer concentration up to 12% in the observed PET image, whereas it remained unaffected in the GM PET image.

TABLE 1. *Influence of the region of interest (ROI) size on quantitation in the observed PET and the GM PET image*

ROI size (pixels)	Observed PET	GM PET
3 ×3	74.5 ± 0.6	121.1 ± 0.9
7 × 7	71.9 ± 2.5	121.1 ± 1.1
11 × 11	70.7 ± 5.1	121.4 ± 1.3
16 × 16	65.8 ± 9.8	121.5 ± 1.4

Analysis on computer simulations as described in Fig. 1. A 3 × 3 MRI pixel ROI was placed in the region of the middle temporal lobe (see Fig. 1). Its size was increased while the position of the center remained fixed. Values are given as mean ± SD.

Error analysis

The effect of possible sources of error on the accuracy of GM PET is demonstrated in Fig. 3A and 3B. Misregistration (but no missegmentation) of the MRI images with respect to the simulated observed PET image by 1 to 3 MRI pixels in either direction resulted in a mean error of 0.4 ± 3.0% (mean ± SD, range of 2.5 to −6%), as indicated by line A in Fig. 3A. Missegmentation of MRI images, resulting in an underestimation of the actual GM volume, produced an overestimation of the true GM concentration. For example, a missegmentation of 2 MRI pixels (corresponding in the presented case of Alzheimer disease to an underestimation of GM volume by 44%) resulted in a 9% overestimation of the actual GM concentration. Missegmentation leading to an overestimation of the actual GM volume produced an underestimation of the true GM concentration. For example, a missegmentation of 1 MRI pixel, corresponding to a 22% overestimation of the actual GM volume, produced an underestimation of the actual GM concentration by 6%. It becomes evident that segmentation and registration errors are additive factors. For a given segmentation error, the lines indicating concomitant misregistration run parallel to line A (misregistration with no missegmentation). Combined errors in registration and segmentation up to 2 MRI pixels did not exceed a 15% inaccuracy in determining the actual tracer concentration in GM.

Misdetermination of the actual WM tracer concentration in the observed PET image was linearly propagated into the GM PET image (Fig. 3B). Given a GM to WM ratio of 4, a 30% over- or underestimation resulted in a 6% under- or overestimation of the actual GM tracer concentration in the GM PET image.

The accuracy of GM PET (defined as recovery of the actual GM tracer concentration) in the presence of inhomogeneous cortical tracer distribution is shown in Fig. 4. It was accurate in cortical foci 3 cm or greater in the anterior–posterior and *z* axis dimension. Between 3 and 0.6 cm, the recovery decreased gradually to 80%, yet remained clearly closer to the actual value than corresponding values in the simulated uncorrected PET image.

Phantom experiments

Sphere phantom. The observed PET image (I_{obs}, Fig. 5a) demonstrated that the recovery of tracer concentration decreases with sphere diameter. Even the largest sphere did not have 100% recov-

ery, as shown in comparison with the full recovery image depicted in Fig. 5b. The weighted summed convolved GM image ($I_{MR_{mod}}$), shown in Fig. 5c, was divided into the observed PET image, yielding the corrected GM PET image ($\tilde{I}_{gray}$), shown in Fig. 5d. The corrected spheres' values demonstrated similar tracer concentrations (24,547 ± 1,909 counts/pixel, mean ± SD, n = 6 spheres; variance within each sphere < 10%), including the smallest one. Most importantly, the tracer concentration was very close in all spheres to the actual apparent tracer concentration of 25,302 ± 2,315 counts/pixel

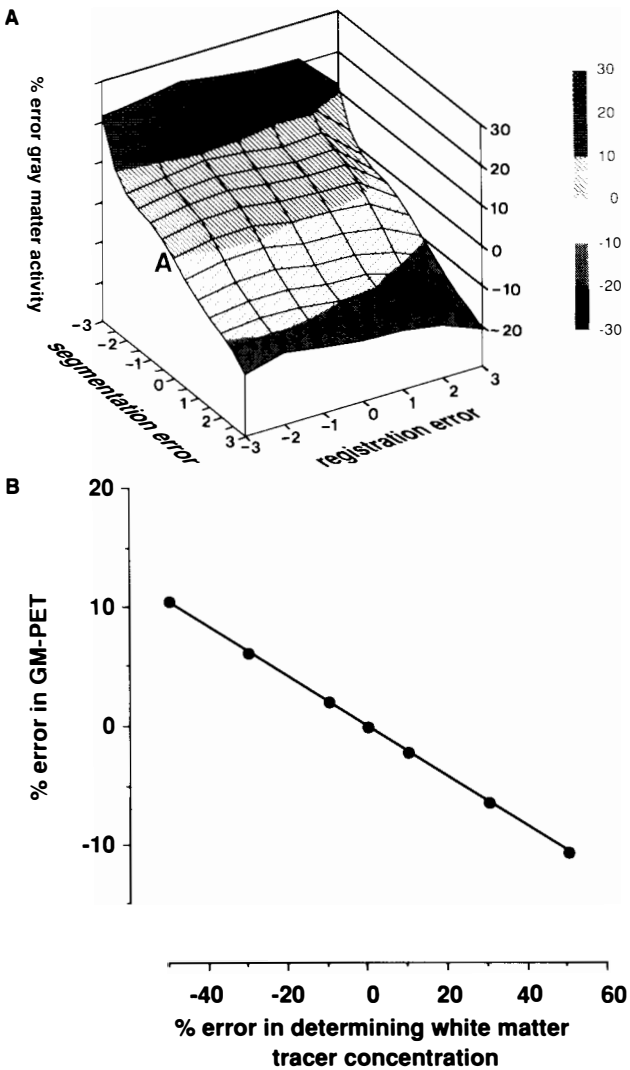

FIG. 3. Error analysis in GM PET—computer simulations on coded MRI images in Alzheimer disease. **(A)** Effects of concomitant misregistration and missegmentation. The data for a given registration error were connected by fifth-order polynomial interpolation (R^2 in all cases ≥0.97), for a given segmentation error by linear interpolation. The units of the x and y axes are number of MRI pixels. **(B)** Misdetermination of the white matter tracer concentration. Errors in determining the actual white matter tracer concentration were propagated into the GM PET image according to $y = -0.16 - 0.21\ x$.

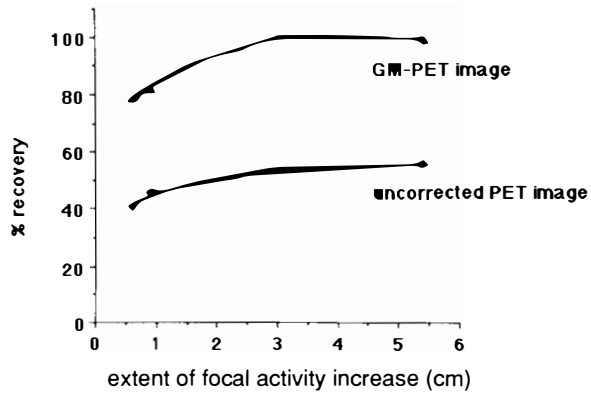

FIG. 4. Effect of regional tracer inhomogeneity on accuracy in GM PET. Quantitation in GM PET was accurate in cortical foci of increased activity, which are 3 cm or greater in the anterior–posterior and z axis dimension and 5–7 mm thick.

as shown in comparison with the full recovery image.

Agarose cortex brain phantom. A representative MRI image is shown in Fig. 6a. The corresponding PET image (I_{obs}) (Fig. 6b) shows a marked decrease in the apparent GM tracer concentration, when compared with the actual concentration, indicated by the full recovery PET image (Fig. 6c). To correct for this partial volume effect, the convolved WM image ($I_{MR_{mod}}$) (Fig. 6d) was subtracted from the observed PET image (Fig. 6b), resulting in $I_{PET_{mod}}$ (not shown). The division of $I_{PET_{mod}}$ by $I_{MR_{mod}}$ (Fig. 6e) yielded the GM PET image (Fig. 6f). The GM PET image had a significantly higher apparent tracer concentration compared to the observed PET image. The tracer distribution was homogeneous. Thin GM regions (e.g., region 1 in Fig. 6a, thickness of 2 mm) showed practically the same tracer concentration as larger areas (e.g., region 2, thickness of 20 mm). A quantitative analysis is summarized in Table 2. Correction for CSF and WM partial volume effects resulted in a more than twofold higher apparent tracer concentration in GM. The GM PET image did recover the actual concentration. The variance of the means decreased from 22.7% before to 4.4% after partial volume correction.

MRI brain tissue segmentation

An example of how human brain tissue can be segmented into GM, WM, and CSF compartments in vivo using MRI is shown in Fig. 7A and 7B for a normal volunteer. The contrast between GM and WM in temporal cortex was 13.4 ± 1.9 (mean ± SD, n = 3 normal volunteers). A quantitative analysis showing the number of MRI pixels with a given signal intensity in a temporoparietal ROI (see Fig. 7A) is shown in Fig. 7B. Four distributions were

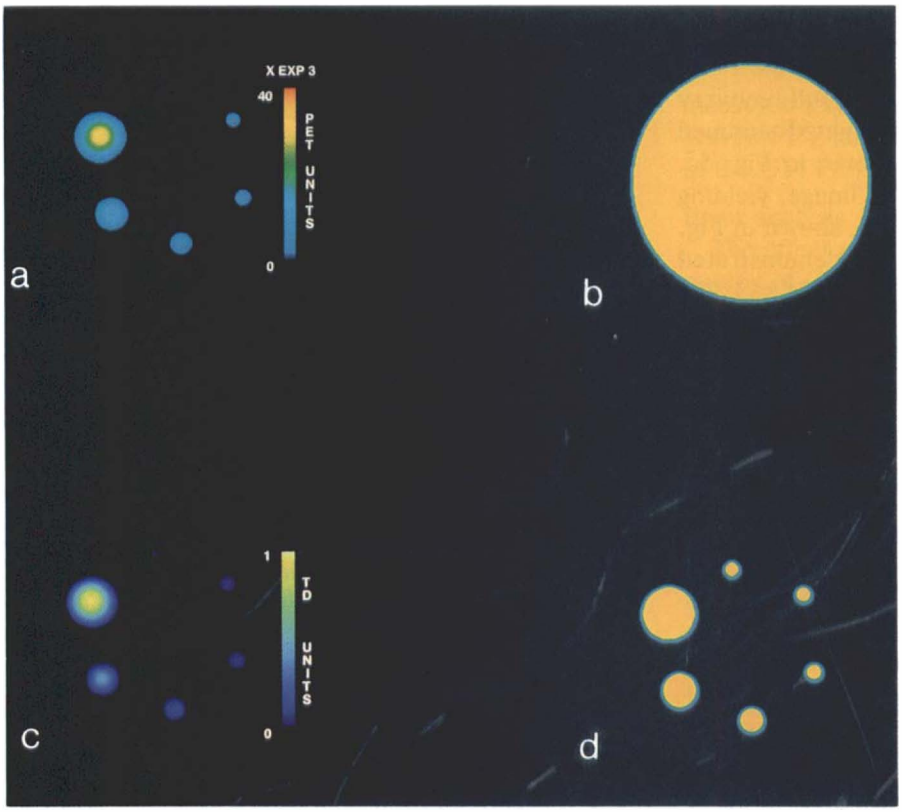

FIG. 5. The implementation of GM PET tested in a sphere phantom. The spheres represent gray matter, and the surrounding space cerebrospinal fluid. Values in Fig. 5a, 5b, and 5d are displayed in PET units (for scale, see Fig. 5a). Values in Fig. 5c are units of weighted gray matter density. **(a)** Observed PET image (I_{obs}) of the sphere phantom. The apparent tracer activity decreases with the sphere diameter. **(b)** Full recovery PET image. Comparing Fig. 5a with 5b shows that even in the biggest sphere, the recovery remains incomplete. **(c)** Convolved weighted summed binarized MRI sphere image ($I_{MR_{mod.}}$). **(d)** GM PET image ($\bar{I}_{gray}$). Dividing the observed PET image (I_{obs}) shown in Fig. 5a by the convolved weighted summed binarized MRI sphere image ($I_{MR_{mod.}}$), demonstrated in Fig. 5c, yields the partial volume-corrected PET image (GM PET image = $\bar{I}_{gray}$). Each sphere now has a similar apparent tracer concentration of 24,547 ± 1,909 counts/pixel (mean ± SD, n = 6 spheres). It corresponds in all spheres to the tracer concentration obtained in the full recovery PET image (25,302 ± 2,315 counts/pixel; Fig. 5b).

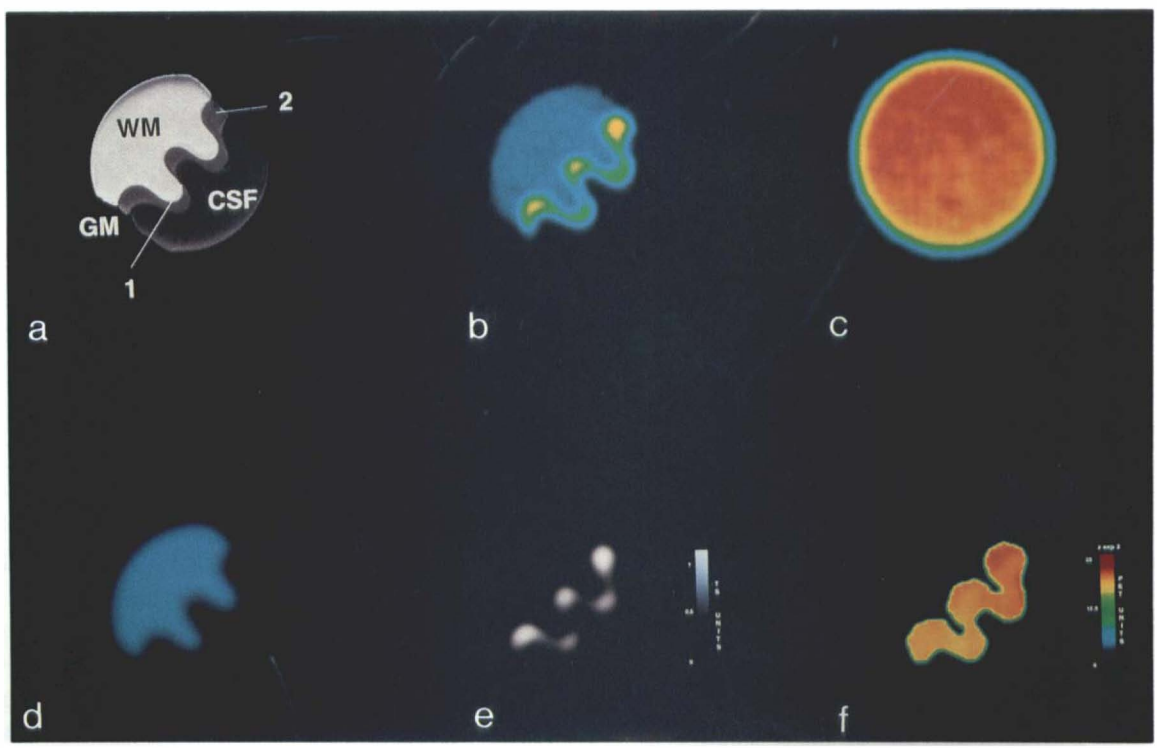

FIG. 6. The implementation of GM PET tested by an agarose brain cortex phantom. Values in Fig. 6a are displayed as MRI units, in Fig. 6b–6d and 6f as PET units (for scale, see Fig. 6f), and values in Fig. 6e as units of weighted gray matter density. **(a)** MRI of the brain cortex phantom. MRI image passing through the center of the phantom. The simulated gray matter thickness varies from 2 (line 1) to 20 mm (line 2). **(b)** Observed PET image (I_{obs}) of the brain cortex phantom. The radioactivity concentration in gray matter was 148 kBq/ml (4 μCi/ml) and in white matter 30 kBq/ml (0.81 μCi/ml) (ratio = 5:1). **(c)** Full recovery PET image. Comparing Fig. 6b with the full recovery image shows a globally decreased and regionally varying recovery in gray matter, depending on the thickness of the gray matter. **(d)** Convolved weighted summed white matter image. Subtraction of this image from the observed PET image (Fig. 6b) yielded the convolved weighted summed gray matter image (not shown). **(e)** Convolved weighted summed binarized MRI gray matter image ($I_{MR_{mod.}}$). **(f)** GM PET image ($\bar{I}_{gray}$). Dividing the convolved weighted summed gray matter image ($I_{PET_{mod}}$) by the convolved weighted summed binarized MRI image ($I_{MR_{mod.}}$) yields the partial volume corrected PET image $\bar{I}_{gray}$. It has a significantly higher and more homogeneous apparent tracer concentration compared to the observed PET image, comparable to the full recovery image (Fig. 6c).

TABLE 2. *Gray matter tracer concentration in the observed PET image and GM PET image simulated in a brain cortex agarose phantom*

	Activity in gray matter	
	Mean ± SD	% Variance
Observed PET (I_{obs})	9,097 ± 2,067	22.7
Full recovery PET	19,416 ± 584	3.0
GM PET	18,918 ± 832	4.4

For details, refer to Fig. 6. Tracer activity is given in counts/pixel.

identified, corresponding to WM, GM, CSF between GM convolutions (CSF_1), and ventricular CSF (CSF_2) as revealed by visual inspection when the MRI pixels under a peak of the histogram are highlighted in the image. Four normal distributions were fitted to the observed data. The goodness of fit of the overall fit as expressed as the RMSE was 0.046. The signal intensity values corresponding to the intersection points of the fitted curves were used as the thresholds between tissue compartments.

Application in a human subject

Figure 8 shows a stepwise demonstration of GM PET in a male human subject with partial complex epilepsy (age of 40 years, onset of seizures at age 26 years). The seizure focus was located in the left anterior temporal lobe, as documented by EEG and later confirmed by the absence of seizures after surgical resection of the left anterior temporal lobe, amygdala, and hippocampus. [^{11}C]carfentanil was used to image μ opiate receptors specifically (Frost et al., 1985). To determine the characteristic function (X) of GM, WM, and CSF, MRI images were acquired and segmented (Fig. 8a to 8c). The images required to perform the partial volume correction according to Eqs. (12) and (14) are shown in Fig. 8d to 8g. Comparison of the resulting GM PET image (Fig. 8j) with the observed PET image (Fig. 8h) shows that the distribution of tracer binding changed. In the observed PET image, the tracer distribution was symmetric in both temporal lobes, whereas it was asymmetric in the GM PET image, with a 20% higher concentration in the left compared to the right anterior temporal lobe.

DISCUSSION

The major finding of this report is that accurate estimation of GM concentrations of PET radiotracers in brain can be made in vivo using a theory that relates the regional fraction of GM to partial volume effect. This method (GM PET) resolves the difficulties due to partial volume effects in measuring radiotracer concentration in relatively small anatomical compartments, and permits near 100% recovery of radiotracer concentration in neocortical GM.

GM has the highest fraction of blood flow (Kameyama et al., 1983), receptor density (Young et al., 1986), and glucose metabolism (Sokoloff et al., 1977; Kameyama et al., 1983), reflecting its paramount role in normal signal processing. Similarly, changes in aging and degenerative brain diseases such as Alzheimer disease are thought to originate in GM (Prohovnik et al., 1989). Accurate measurement of physiological and biochemical processes and their alterations, specifically in GM in vivo, is therefore desirable. Currently, the biological impli-

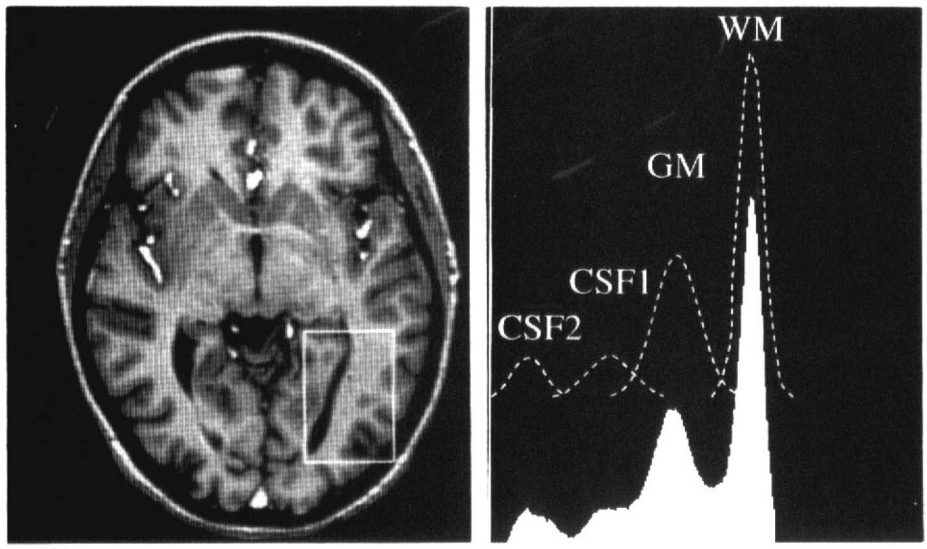

FIG. 7. In vivo brain tissue segmentation into gray matter, white matter, and cerebrospinal fluid compartments using MRI. **(A)** Transaxial MRI brain image. The region of interest in the temporoparietal area was used for the histogram shown in Fig. 7B. **(B)** A histogram of the posterior temporoparietal area, showing the number of MRI pixels with a given signal intensity (white area). Four peaks can be identified, corresponding to white matter (WM), gray matter (GM), cerebrospinal fluid between gray matter convolutions (CSF_1), and ventricular cerebrospinal fluid (CSF_2). Four normal distributions were fitted to the data (dotted line). The intersection of two adjacent fitted normal distributions was taken to segment the corresponding two compartments.

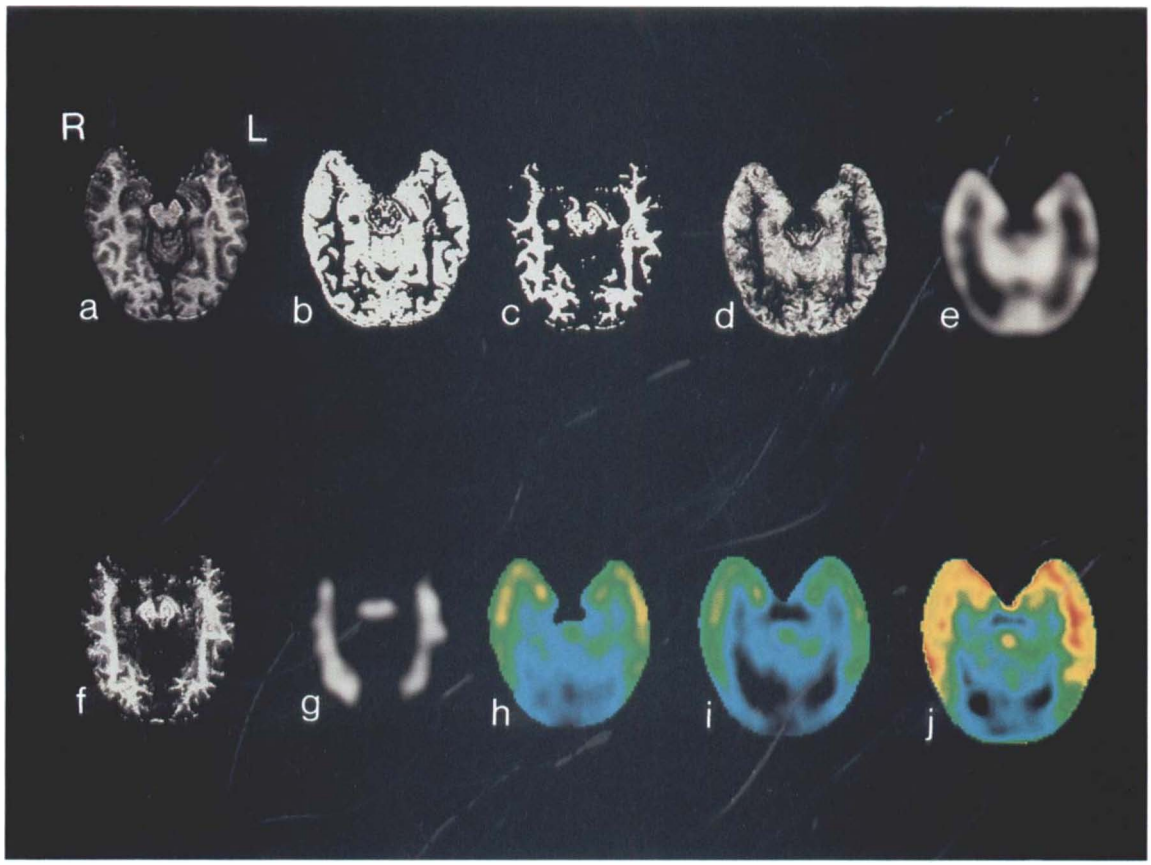

FIG. 8. GM PET of μ opiate receptors in a patient with left-sided temporal lobe epilepsy using [^{11}C]carfentanil. Values in Fig. 8h–j are displayed to the same scale. **(a)** T_1-weighted spoiled grass (SPGR) MRI image. **(b)** Segmented gray matter image. **(c)** Segmented white matter image. **(d)** Summed segmented gray matter images. **(e)** Convolved segmented gray matter images. Note that the density of gray matter tissue in the left anterior temporal lobe is lower compared to the right side. **(f)** Summed segmented white matter images. **(g)** Convolved segmented white matter images. **(h)** Observed PET image (I_{obs}). Symmetric distribution of [^{11}C]carfentanil binding to μ opiate receptors in temporal lobe. **(i)** PET image of the gray matter ($I_{PET_{mod}}$), obtained by subtracting the convolved weighted summed white matter image (Fig. 8g) from the observed PET image. **(j)** GM PET image ($\bar{I}_{gray}$). Result of dividing $I_{PET_{mod}}$ by $I_{MR_{mod}}$. The image shows a global increase in the apparent tracer concentration. More importantly, [^{11}C]carfentanil binding to the left anterior temporal lobe is now higher when compared to the right anterior temporal lobe.

cation of a change in the apparent tracer concentration in PET may be equivocal. Changes might reflect exclusively a change in GM, WM, or CSF *volume*. For example, simulations on coded MRI images revealed that neocortical GM thinning by 3 mm without change in the actual tracer concentration reduces the apparent tracer concentration in the uncorrected PET image by 30% (FWHM between 5 and 12 mm, data not shown). A change in an apparent tracer concentration in PET may also reflect a specific alteration of a physiological or biochemical process *per unit volume* of GM or WM. GM PET offers a way to differentiate between these possibilities.

After partial volume correction, the mean apparent activity in the GM compartments was practically identical to actual values, demonstrating the accuracy of GM PET. The studies thus show that the assumptions made in the theory and its implementation are appropriate. In the simulation studies, brain anatomy was precisely reproduced by using actual human MRI data. The activity gradient between GM and WM was similar to corresponding gradients encountered in autoradiographic studies of glucose metabolism (Sokoloff et al., 1977), both in computer simulations and the brain phantom. However, in the latter, neocortical anatomy was only approximately replicated. More realistic agarose brain phantoms will need to be constructed to evaluate thoroughly the method in various cases of cortical anatomy and for subcortical structures.

The impact of registration errors encountered in routine image processing (Pelizzari et al., 1989) on accuracy of GM PET and the effects of misdetermining the WM concentration in the centrum semiovale by 50% did not exceed 10%. Errors induced by missegmentation of WM and GM by 0.94 to 2.8 mm ranged between 1 and 25%. Although not ex-

plicitly addressed, it is evident that the same applies to errors in segmentation of CSF space and GM. Thus, GM PET is relatively sensitive to inaccuracies in determining the GM volume. This can analytically be anticipated by realizing the relatively small thickness of the cortical GM and by considering that the segmented GM compartment constitutes the denominator of Eq. (14) used to compute the GM PET image.

Accuracy in in vivo segmentation of brain tissue has significantly improved by recent advances in MRI, and SPGR pulse sequences result with short imaging times and a high contrast between WM, GM, and CSF. Nevertheless, the existence of a certain number of "mixed" pixels due to partial volume effects in the MRI images remains an issue that needs to be addressed using various segmentation algorithms and phantoms. In the present study, a relatively simple approach was chosen by assuming a normal distribution of signal intensity values in each compartment. Although normal distributions fit the observed histograms well, these studies need to be extended. The distribution of signal intensity values in brain diseases might vary. More complex techniques such as Bayesian classification, relaxation labeling, neural networks, and Markov random fields (Van Trees, 1968; Rosenfeld et al., 1976; Geman and Geman, 1984; Frederick, 1990) are available, and might need to be considered as a means to increase accuracy and precision further in tissue segmentation. In addition, due to magnetic field inhomogeneity, threshold values derived from one region might not be correct in another, and this can be addressed by performing a series of "regional" segmentations with attention to continuity across regions. Ultimately, the approach needs to be validated in nonhuman primates where both tissue compartment size and GM concentration can be determined ex vivo.

The algorithm of GM PET assumes a homogeneous tracer distribution in WM. In receptor autoradiography, this assumption has been shown to be valid in vitro for most receptors that are predominantly located in GM (Young et al., 1986). In vivo, this issue has been addressed for μ opiate receptors. Inhibition of the specific binding of [^{11}C]carfentanil to μ opiate receptors (present in GM, but very low in WM) by naloxone resulted in a low and homogeneous tracer distribution throughout brain tissue in normal volunteers, demonstrating a homogeneous tracer distribution in the WM compartment in vivo (Frost et al., 1985).

The activity in the CSF space was assumed to be zero, both in computer simulations and in the human study. In normal subjects, it would be difficult to measure ventricular radioactivity in PET studies without significant inaccuracy due to partial volume effects. Patients with enlarged ventricles or ventricular shunts might present an opportunity to investigate further whether CSF activity is best approximated as zero, WM, or some value in between. The GM PET algorithm provides a term to correct for nonzero CSF concentration [I_{CSF}, see Eqs. (4) and (10)]. Nevertheless, a relatively large error in low activity compartments will result in a small inaccuracy in GM PET, as shown in the WM simulations. The relationship of WM, ventricular, and sulcal CSF activity would be expected to vary with time, but GM PET could be performed at multiple time points when kinetic studies are required.

The GM PET algorithm is analytically correct when either the point spread function of the PET instrument is a delta function or the radioactivity distribution within GM is homogeneous. Because the first criterion is not met, the algorithm requires the latter. In practice, inhomogeneity will occur, and its effect on the accuracy of GM PET needs to be known. Simulation studies of GM PET showed that quantitation is 95% accurate when the size of a region of 30% increased activity measures 2 cm in the anterior–posterior and axial dimensions. This size is sufficient to measure regional cortical activity accurately in most clinical and research studies, including activation studies by visual presentation of words (Petersen et al., 1990). As the spatial resolution improves, and more closely approximates a delta function, GM PET will tolerate greater focal inhomogeneity.

GM PET has been applied to human PET data in a feasibility study. The method works well and, interestingly, demonstrated a regional increase in [^{11}C]carfentanil binding in a patient with temporal lobe epilepsy not evident in the uncorrected image. This preliminary finding encourages a more widespread application of the method and is consistent with previous studies showing an increase in [^{11}C]carfentanil binding in 75% of patients with temporal lobe epilepsy on the side of the electrical focus (Frost et al., 1988; Mayberg et al., 1991).

In conclusion, GM PET is accurate in determining a radiotracer concentration per unit GM in neocortex in vivo. The well-recognized difficulties in interpreting PET images due to the anatomical variability of the cortex within a subject and in comparisons between subjects can thus be reduced. The function of brain areas with localized cerebral atrophy (Goulding et al., 1989) can now be more accurately studied. Although the present study has focussed on brain GM, the theory and implementation involved could readily be modified such that other

body compartments, such as the heart, can be corrected for partial volume effects. GM PET thus presents a generally applicable approach to partial volume-corrected functional imaging of relatively small anatomical compartments.

Acknowledgment: The authors thank K. W. Leong, Ph.D. and B. Reisfeld, Ph.D. for assistance in constructing the agarose brain cortex phantom; R. F. Dannals, Ph.D., A. A. Wilson, Ph.D., and H. T. Ravert, Ph.D. for radiotracer synthesis; C. C. Meltzer, M.D. for helpful discussions; C. C. Cromwell, B.A. for assistance in data processing; D. Clough, CNMT for PET scan acquisition and processing; A. W. Kimball, Ph.D. for statistical consultation; and W. Zeffiro for editorial suggestions. This study was supported by U.S.P.H.S. grants AG08740 and NS 15080, and the Deutsche Forschungsgemeinschaft (Mu 735/2-2).

REFERENCES

Chawluk JB, Alavi A, Dann R (1987) Positron emission tomography in aging and dementia: Effect of cerebral atrophy. *J Nucl Med* 28:431–437

Chawluk JB, Dann R, Alavi A, Hurtig HI, Gur RE, Resnick S (1990) The effect of focal cerebral atrophy in positron emission tomographic studies of aging and dementia. *Nucl Med Biol* 17:797–804

Condon B, Wyper D, Grant R (1986) Use of magnetic resonance imaging to measure intracranial cerebrospinal fluid volume. *Lancet* 1:1355–1357

Foster NL, Chase TM, Fedio P, Patronas NJ, Brooks RA, DiChiro G (1983) Alzheimer's disease, focal cortical changes shown by positron emission tomography. *Neurology* 33:961–965

Fowler JS (1990) Enzyme activity: Monoamine oxidase. In: *Quantitative Imaging—Neuroreceptors, Neurotransmitters, and Enzymes* (Frost JJ, Wagner HN Jr, eds), New York, Raven Press, pp 179–192

Frederick B (1990) Implementation and evaluation of a neural network algorithm for magnetic resonance image segmentation. Proceedings of SPIE Conference on Medical Imaging IV, Newport Beach, CA

Frost JJ (1986) Imaging neuronal biochemistry by emission computed tomography: Focus on neuroreceptors. *Trends Pharmacol Sci* 7:490–496

Frost JJ, Wagner HN Jr, eds (1990) *Quantitative Imaging—Neuroreceptors, Neurotransmitters, and Enzymes*. New York, Raven Press

Frost JJ, Wagner HN Jr, Dannals RF, Ravert HT, Links JM, Wilson AA, Burns HD, Wong DF, McPherson RW, Rosenbaum AE, Kuhar MJ, Snyder SH (1985) Imaging opiate receptors in the human brain by positron tomography. *J Comput Assist Tomogr* 9:231–236

Frost JJ, Mayberg HS, Fisher RS, Douglass KH, Dannals RF, Links JM, Wilson AA, Ravert HT (1988) Mu-opiate receptors measured by positron emission tomography are increased in temporal lobe epilepsy. *Ann Neurol* 23:231–237

Geman S, Geman D (1984) Stochastic relaxation using Gibbs distributions, and the Bayesian restoration of images. *IEEE J Patt Anal Mach Intell* 6:721–741

Goulding PJ, Northen B, Snowden JS, MacDermott N, Neary D (1989) Progressive aphasia with right-sided extrapyramidal signs: Another manifestation of localised cerebral atrophy. *J Neurol Neurosurg Psychiatry* 52:128–130

Henkelman RM (1985) Measurement of signal intensities in the presence of noise in MR images. *Med Phys* 12:232–233

Herscovitch P, Auchus AP, Gado M, Chi D, Raichle ME (1986) Correction of positron emission tomography data for cerebral atrophy. *J Cereb Blood Flow Metab* 6:120–124

Hoffmann EJ, Huang SC, Phelps ME (1979) Quantitation in positron emission computed tomography: 1. Effect of object size. *J Comput Assist Tomogr* 3:299–308

Kameyama M, Wasterlain C, Ackermann R, Finch D, Lear J, Kuhl D (1983) Neuronal response of the hippocampal formation to injury: Blood flow, glucose metabolism, and protein synthesis. *Exp Neurol* 79:329–346

Kessler RM, Ellis JR, Eden M (1984) Analysis of emission tomographic scan data: Limitations imposed by resolution and background. *J Comput Assist Tomogr* 8:514–522

Koeppe RA, Rosenthal G, Gilman S, Lopez R, Junck L, Gebarski SS (1989) Correction for effects of tissue atrophy in PET studies using quantitative anatomic imaging [Abstract]. *J Cereb Blood Flow Metab* 9(suppl 1):S197

Kohn MI, Tanna NK, Herman GT, Resnick SM, Mozley PD, Gur RE, Alavi A, Zimmerman RA, Gur RC (1991) Analysis of brain and cerebrospinal fluid volumes with MR Imaging. Part I. Methods, reliability, and validation. *Radiology* 178: 115–122

Kuhl DE, Metter EJ, Riege WH, Markham CH (1982) Effects of human aging on patterns of local cerebral glucose utilization determined by (^{18}F) fluorodeoxyglucose method. *J Cereb Blood Flow Metab* 2:163–171

Leenders KL, Perani D, Lammertsma AA, Heather JD, Buckingham P, Healy MJR, Gibbs JM (1990) Cerebral blood flow, blood volume, and oxygen utilization: Normal values and the effect of age. *Brain* 113:27–47

Martin AJ, Friston KJ, Colebatch JG, Frackowiak RSJ (1991) Decreases in regional cerebral blood flow with normal aging. *J Cereb Blood Flow Metab* 11:684–689

Mayberg HS, Sadzot B, Meltzer CC, Fisher RS, Lesser RP, Dannals RF, Lever JR (1991) Quantification of mu and non-mu opiate receptors in temporal lobe epilepsy using positron emission tomography. *Ann Neurol* 30:3–11

Meltzer CC, Leal JP, Mayberg HS, Wagner HN Jr, Frost JJ (1990*a*) Correction of PET data for partial volume effects in human cerebral cortex by MR imaging. *J Comput Assist Tomogr* 14:561–570

Meltzer CC, Bryan RN, Holcomb HH, Kimball AW, Mayberg HS, Sadzot B, Leal JP, Wagner HN Jr, Frost JJ (1990*b*) Anatomical localization for PET using MR imaging. *J Comput Assist Tomogr* 14:418–426

Mitchell MD, Kundel HL, Axel L, Joseph PM (1986) Agarose as a tissue equivalent phantom material for NMR imaging. *Magn Reson Imag* 4:263–266

Müller-Gärtner HW, Mayberg HS, Ravert HT, Dannals RF, Wilson AA, Tune L, Brandt J, Frost JJ (1991) Mu opiate receptor binding in amygdala in Alzheimer's: In vivo quantification by ^{11}C carfentanil and PET [Abstract]. *J Cereb Blood Flow Metab* 11(suppl 2):S20

Pelizzari CA, Chen GTY, Spelbring DR, Weichselbaum RR, Chen CT (1989) Accurate three-dimensional registration of CT, PET, and/or MR images of the brain. *J Comput Assist Tomogr* 13:20–26

Penn RD, Belanger MG, Yasnoff MD (1978) Ventricular volume in man computed from CAT scans. *Ann Neurol* 3:216–223

Petersen SE, Fox PT, Snyder AZ, Raichle ME (1990) Activation of extrastriate and frontal cortical areas by visual words and word-like stimuli. *Science* 249:1041–1044

Phelps ME, Mazziotta JC (1985) Positron emission tomography: Human brain function and biochemistry. *Science* 228:799–809

Prohovnik I, Smith G, Sackheim HA, Mayeux R, Stern Y (1989) Gray-matter degeneration in presenile Alzheimer's disease. *Ann Neurol* 25:117–124

Rabins PV, Pearlson GD, Aylward E, Kumar AJ, Dowell K (1991) Cortical magnetic resonance imaging changes in elderly inpatients with major depression. *Am J Psychiatry* 148: 617–620

Rosenfeld A, Hummel RA, Zucker SW (1976) Scene labeling by

relaxation operations. *IEEE J Man Mach Cybernet* 6:420–433

Seab JP, Jagust WJ, Wong STS, Roos MS, Reed BR, Budinger TF (1988) Quantitative NMR measurements of hippocampal atrophy in Alzheimer's disease. *Magn Reson Imag* 8:200–208

Sokoloff L, Reivich M, Kennedy C, Des Rosiers CS, Patlak CS, Pettigrew KD, Sakurada O, Shinohara M (1977) The (^{14}C)deoxyglucose method for the measurement of local cerebral glucose utilization: Theory, procedure and normal values in the conscious and anesthetized albino rat. *J Neurochem* 28:897–916

Tanna NK, Kohn MI, Horwich DN, Jolles PR, Zimmerman RA, Alves WM, Alavi A (1991) Analysis of brain and cerebrospinal fluid volumes with MR imaging: Impact on PET data correction for atrophy. Part II. Aging and Alzheimer dementia. *Radiology* 178:123–130

Valk PE, Jagust WJ, Derenzo SE, Huesman RH, Geyer AB, Budinger TF (1990) Clinical evaluation of a high-resolution (2.6-mm) positron emission tomography. *Radiology* 176: 783–790

Van Trees HL (1968) *Detection, Estimation, and Linear Modulation Theory: Part I.* New York, John Wiley & Sons

Videen TO, Permutter JS, Mintun MA, Raichle ME (1988) Regional correction of positron emission tomography data for the effects of cerebral atrophy. *J Cereb Blood Flow Metab* 8:662–670

Wagner HN Jr, Burns HD, Dannals RF (1983) Imaging dopamine receptors in the human brain by positron tomography. *Science* 221:1264–1266

Wyper DJ, Pickard JD, Matheson M (1979) Accuracy of ventricular volume estimation. *J Neurol Neurosurg Psychiatry* 42: 345–350

Yamaguchi T, Kanno I, Uemura K, Shishido F, Inugami A, Ogawa T, Murakami M, Suzuki K (1986) Reduction in regional cerebral metabolic rate of oxygen during human aging. *Stroke* 17:1220–1228

Yoshii F, Barker WW, Chang JH, Loewenstein D, Apicella A, Smith D, Boothe T, Ginsberg MD (1988) Sensitivity of cerebral glucose metabolism to age, gender, brain volume, brain atrophy, and cerebrovascular risk factors. *J Cereb Blood Flow Metab* 8:654–661

Young AB, Frey KA, Agranoff BW (1986) Receptor assays: *In vitro* and *in vivo*. In: *Positron Emission Tomography and Autoradiography—Principles and Applications for the Brain and Heart* (Phelps ME, Mazziotta JC, Schelbert HR, eds), New York, Raven Press, pp 73–111